


Review

Resonant Airborne Acoustic Emission for Nondestructive Testing and Defect Imaging in Composites

Igor Solodov , Yannick Bernhardt and Marc Kreutzbruck

IKT, University of Stuttgart, 70569 Stuttgart, Germany; yannick.bernhardt@ikt.uni-stuttgart.de (Y.B.); marc.kreutzbruck@ikt.uni-stuttgart.de (M.K.)

* Correspondence: igor.solodov@ikt.uni-stuttgart.de

Abstract: A new version of an acoustic emission mode which is different from its traditional counterpart is discussed in view of applications for nondestructive testing. It is based on the effect of acoustic waves generation from the defect area in ambient air by local standing wave vibration developed in this area at the defect resonant frequency. Another approach which does not require preliminary knowledge of local defect-resonance frequency is one that uses wideband acoustic activation by a noise-like input signal. The acoustic emission field from the defect area is a “fingerprint” of the radiation source, and thus is applicable to defect detection and imaging. This enables the use of commercial microphone scanning for detecting and imaging various defects in composites. An improvement in the acoustic-emission scanning mode based on a multiple-axis robot is studied to applications to complex shape components. A rapid, full-field imaging of the acoustic-emission field is implemented by means of an array of microphones (acoustic camera). Numerous case studies validate the potential of the resonant acoustic-emission modes for integration in the defect imaging system based on inexpensive, fully acoustic instrumental components.



Citation: Solodov, I.; Bernhardt, Y.; Kreutzbruck, M. Resonant Airborne Acoustic Emission for Nondestructive Testing and Defect Imaging in Composites. *Appl. Sci.* **2021**, *11*, 10141. <https://doi.org/10.3390/app112110141>

Academic Editors: Dimitrios Aggelis and Antolino Gallego

Received: 28 September 2021

Accepted: 27 October 2021

Published: 29 October 2021

Publisher's Note: MDPI stays neutral with regard to jurisdictional claims in published maps and institutional affiliations.



Copyright: © 2021 by the authors. Licensee MDPI, Basel, Switzerland. This article is an open access article distributed under the terms and conditions of the Creative Commons Attribution (CC BY) license (<https://creativecommons.org/licenses/by/4.0/>).

Keywords: Local Defect Resonance; Resonant Air-Coupled Emission; acoustic camera

1. Introduction

The forecast for the global market of lightweight, fibre-reinforced composite materials projects about 40% growth by 2024 due to increasing demands in aerospace and transportation industries [1]. In these safety-relevant applications, an assessment of the probability of failure is necessary for individual components and entire systems. Because of the often-manual manufacturing of composite components, the structural parts have to go through 100% nondestructive testing (NDT). A commonly used method is an ultrasonic inspection by using an array of multiple elements to scan over the whole specimen area. However, with the increasing use and field applications of fibre-reinforced composites, new NDT methods have to be promoted and must shape up to these new materials.

Acoustic emission (AE) is an established NDT method based on monitoring transient, elastic wave packages in a material, which accompany irreversible changes (cracking, microfracture) in its internal structure [2]. The AE events are then detected by acoustic wave transducers attached to the specimen. To locate the damage, the transducers are set in arrays and the beamforming computation tool is applied [3]. Acoustic emission has several advantages, including inspection of large components and the capability to determine the location of damage. The downside is that the component must be further damaged to generate the AE signal.

Owing to elastic coupling with ambient air, acoustic waves that hit the surface of the solid produce airborne sound. As a result, conventional (internal) AE is accompanied by airborne (external) AE events, which can be received remotely, e.g., by air-coupled transducers [4]. A similar beamforming approach that uses an array of acoustic microphones (acoustic camera) is further applied to locate and detect the airborne sound sources [5].

However, commercial acoustic cameras are barely applicable to the detection of ultrasound, since they mainly operate in audible frequency ranges [6,7].

The efficiency of the airborne sound radiation is expected to rise, provided that a standing wave resonance develops in the subsurface source. Such an approach to the enhancement of acoustic responses of defects in composites was proposed by using frequency-selective acoustic activation based on the concepts of Local Defect Resonance (LDR) [8] and Resonant Air-Coupled Emission (RACE) [9]. In this paper, the effect of RACE is assessed as a background of a new mode of AE in view of applications for NDT and defect imaging in composites. The AE imaging is achieved by using different mechanical scanning units: a three-axis-scanning table and a six-axis industrial robot. A new approach to instant, full-field ultrasound defect imaging is proposed by using an acoustic camera. Adapting acoustic cameras to sound-field imaging enables researchers to save testing time and to make progress in the development of new, fully acoustic methods for NDT of composite materials.

2. LDR & RACE: Background & Simulation

In the last decade, the LDR approach has created a great deal of interest and progress in research on the applications of new resonant techniques for NDT and defect imaging in composites [10–15]. The concept of LDR is based on the fact that material damage is accompanied by a local decrease in stiffness for a certain material mass. By lumping the distributed vibration parameters into equivalent mass and stiffness, the damaged area, therefore, can be modelled as an oscillator with natural frequency $f_0 = \frac{1}{2\pi} \sqrt{K_{eff}/M_{eff}}$, where K_{eff} is the effective material rigidity and M_{eff} is the vibrating mass of the defect.

This phenomenology can be readily extended to more rigorous analytics for planar defects (e.g., flat bottomed holes (FBH) or delaminations) in composites [16]. Like in the classical resonance interpretation, the LDR can be then perceived as an outcome of a standing wave formation due to constructive interference of the flexural waves inside the defect which results in the fundamental resonance frequency $f_0 = (v/2L)F$, where v is the wave velocity, L is the size parameter of the defect and F is the defect shape factor.

The flexural wave velocity depends on frequency f and is known to have a closed form expression [17]:

$$v = (Eh^2/12\rho(1 - \mu^2))^{1/4} \omega^{1/2} \quad (1)$$

where E is the material Young's modulus, ρ is its density, μ is Poisson's ratio, h is the plate thickness and $\omega = 2\pi f$.

At the resonance $f = f_0$ in (1), and after substitution of $v(f_0)$ into the above expression, one obtains [16]:

$$f_0 = \frac{\pi}{4\sqrt{3}} \frac{h}{L^2} F^2 \sqrt{\frac{E}{\rho(1 - \mu^2)}} \quad (2)$$

Besides the numerical factor, Equation (2) demonstrates the generic structure of the analytical expressions for LDR frequency. The characteristic square-root term in (2) specifies the dependence of the material properties on the plate bending stiffness, $D = Eh^3/12(1 - \mu^2)$. The general sizing term (h/L^2) indicates a linear increase in the resonance frequency with the depth of the defect, which is reciprocal to the defect area. The calculations from (2) show that for cm-size defects in composites, the LDR frequencies are usually in the kHz-frequency range, while the coupling to ambient air must be accompanied by the airborne acoustic radiation.

To substantiate the effect of RACE and its connection to LDR, the results of FEM simulation of the resonant behaviour of defects (circular and rectangular FBH) by using COMSOL multiphysics software are shown in Figure 1a–c.

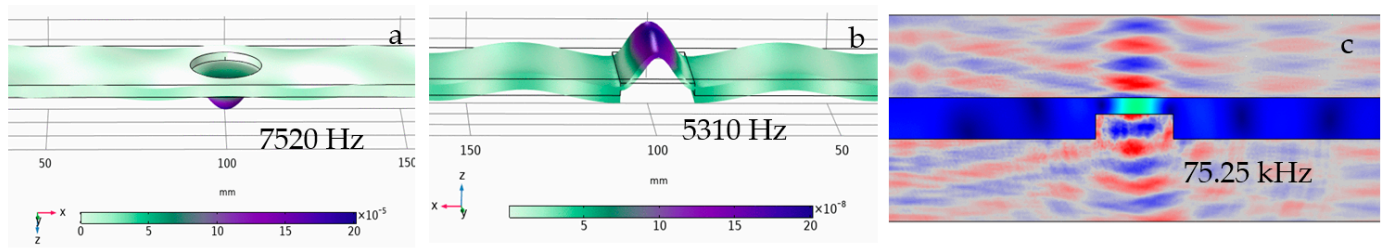


Figure 1. (a–c): FEM simulation of resonant behaviour of FBH: LDR for a circular (a) and rectangular (b) FBH in polymethyl methacrylate (PMMA); (c) RACE for rectangular FBH in an aluminium plate.

The simulations in Figure 1a,b are based on Eigenfrequency Analysis in the Structural Mechanics Module (triangular elements, fine mesh, frequency step 10 Hz), that essentially calculates the idealised specimen-vibration patterns at various natural frequencies in vacuum (no acoustic coupling to ambient air). The standing wave LDR of the defects are clearly manifested at certain frequencies: the fundamental LDR frequency corresponds to a half-wave resonance with the vibration node at the defect boundary line. This provides an enclosure of the LDR field: the nodal line along the defect contour “locks” the resonant excitation within the damage area, and a strong vibration of the defect nonradiating to the rest of the specimen is observed.

To include the airborne acoustic coupling of the LDR-induced vibrations, the COMSOL calculations comprised an additional acoustic module, resulting in Figure 1c, which shows a clear airborne radiation from the defect area at the LDR frequency. Since the wavelength in air is substantially smaller than that in solid at the same frequency, the airborne wave field remains similar to a plane wave pattern (near-field zone) at moderate distances from the surface. The RACE signal is, therefore, well-suited for detecting and visualization of defects by revealing their external AE with a distant acoustic wave receiver.

3. RACE Experimental Evidence

In the experiments, commercial piezo-actuators manufactured by isi-sys GmbH with a frequency response extended into the 100–200 kHz range were used for activation of defects. To recognise the LDR frequency, the voltage applied is in chirp mode (bandwidth above 100 kHz, input 10–20 V) from the HP 33120A arbitrary waveform generator after the HVA-B100 amplifier.

The RACE signal is detected by a half-inch condenser microphone (B&K 4130, sensitivity 10 mV/Pa) combined with 40 dB preamplifier type B&K 2642 and power supply B&K 2810, positioned at a close distance above the specimen surface and attached to a 2D scanner (Isel-automation) (Figure 2).

To investigate the RACE field features, the simulated defects of circular-shaped Flat-Bottom Holes (FBH) (different radii and residual back-wall thicknesses) in PMMA plates were used. A close interconnection between RACE and LDR is obvious from Figure 3: the RACE signal closely matches the frequency response of LDR. The latter is measured for a wideband excitation of FBH by using a laser vibrometer (PSV 300 Polytec, Waldbronn, Germany) and is compared with microphone RACE response at different frequencies.

Another way to detect and visualize the RACE is concerned with application of the air-coupled vibrometry [18]. The technique is based on a focused laser beam which propagates through the airborne field created by the wave in the solid specimen, is then reflected from a fixed reflector, and is processed by a heterodyne interferometer of the laser vibrometer Polytec 300. Due to the photoelasticity of air, the optical path length of the beam and its frequency are modulated according to the airborne acoustic pressure. The induced frequency shift is recognized by the vibrometer software as a variation in vibration velocity of the sound in air that is visualized and measured.

The use of the air-coupled vibrometry in imaging RACE from point-of-impact damage (indicated by the white circle, Figure 4a) in a carbon fibre-reinforced polymer (CFRP) is illustrated in Figure 4b,c, which provides side views of a laser vibrometer C-scan of the air

above the surface of the CFRP. In a separate measurement, laser vibrometry reveals LDR in the small, damaged area at 110 kHz. When excited at a frequency outside of LDR (90 kHz, Figure 4b), the point impact does not affect the wave propagation, and the airborne field is a slanted plane wave propagating at an angle defined by the ratio of the sound velocities in air and in the specimen.

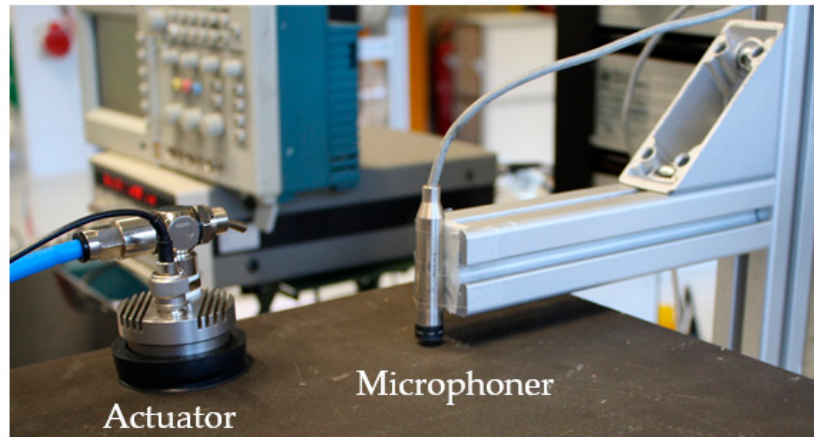


Figure 2. Setup for excitation and microphone RACE detection and defect imaging.

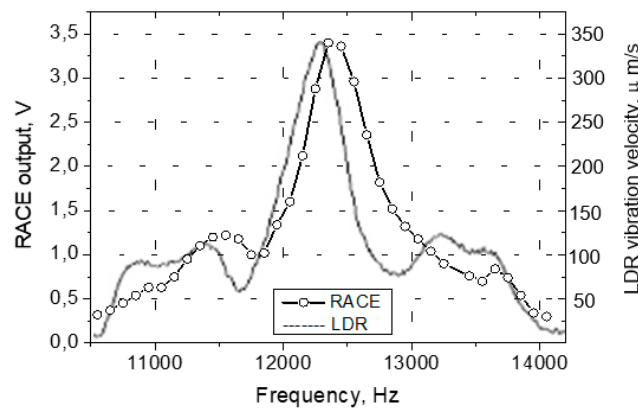


Figure 3. Comparison of RACE and LDR frequency responses for FBH in PMMA plates.

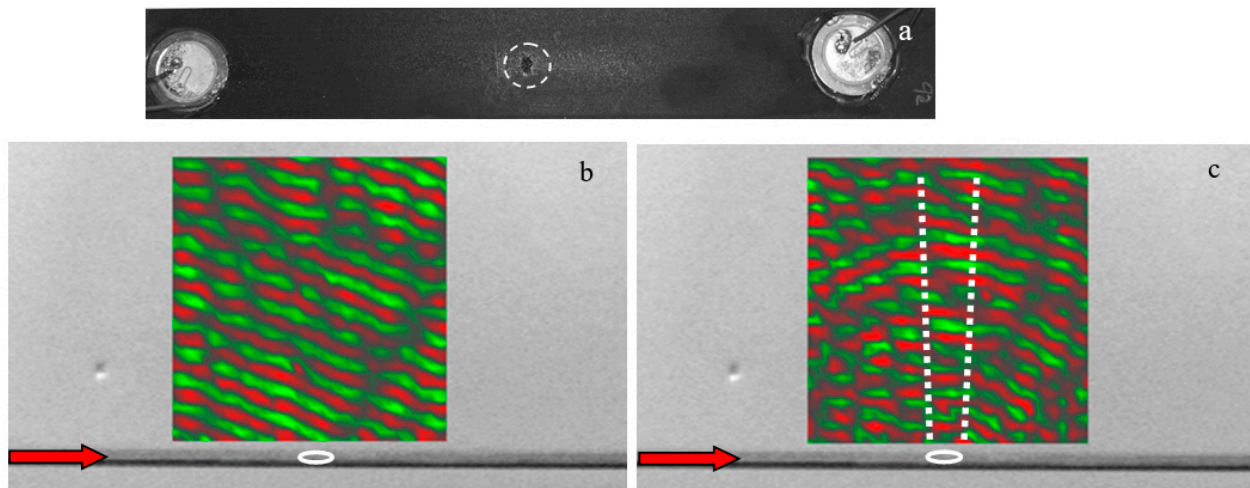


Figure 4. The point of impact in the CFRP specimen studied (a); airborne field above the CFRP specimen with an impact: (b) nonresonant case (90 kHz excitation); (c) LDR-induced RACE at 110 kHz excitation.

The airborne field changes dramatically when the wave frequency coincides with LDR frequency (110 kHz) (Figure 4c): the radiation from the defect area turns into a spherical wave at a distance of a few wavelengths from the defect (far field). In the near-field zone, a part of the wave front could be considered as an airborne “fingerprint” of the defect, emitted in the vertical direction (inside the dotted area in Figure 4b). The near-field part of radiation is preferable for receiving the RACE signal and imaging of the defect.

This conclusion is also apparent from another RACE evidence experiment shown in Figure 5. An impact-induced damage ($15 \times 7 \text{ mm}^2$) (Figure 5a, reverse side) in a CFRP plate ($165 \times 30 \times 2.5 \text{ mm}^3$) manifests LDR at 59,500 Hz. The air-coupled vibrometry image taken outside the LDR frequency (b) indicates a conventional standing wave pattern radiation with $\lambda/2$ shifts in adjacent areas. At the LDR frequency, the radiation changes for quasi-plane-wave RACE in the near-field zone (c), which is an airborne “cast” of the same size as the defect area, clearly seen after averaging in the Root-Mean-Square (RMS) mode (d).

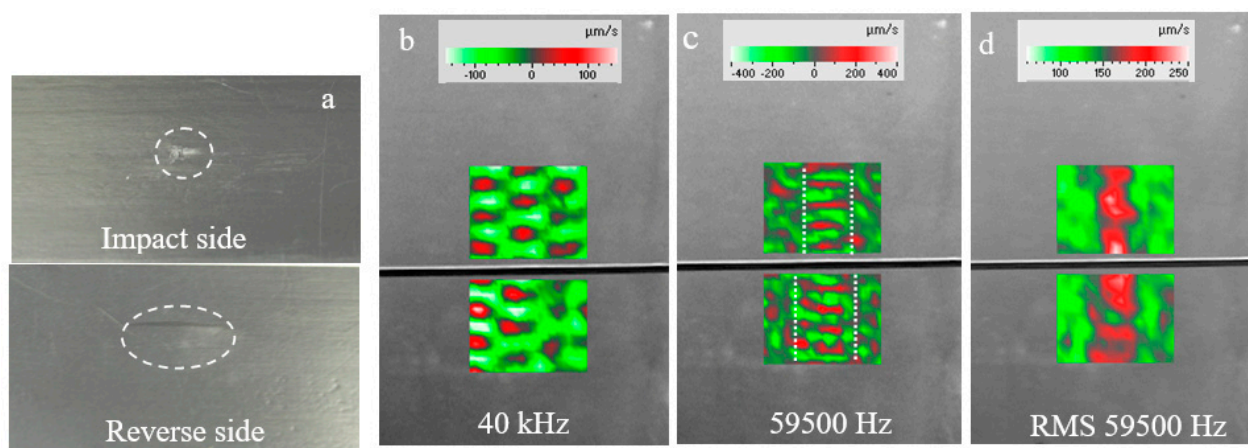


Figure 5. Airborne AE from impact damage in CFRP plate (a): standing wave pattern at 40 kHz (b); RACE at LDR frequency (c,d).

4. RACE Scanning Mode

As shown above, the RACE signal is a footprint of the airborne emission from the damaged area, and therefore, can be employed naturally for its imaging [19]. An example of the RACE application to damage imaging is shown in Figure 6 for a heat-induced, elliptical, local defect in the CFRP plate ($300 \times 300 \times 4 \text{ mm}^3$) Figure 6a. LDR frequency for ($\approx 10 \times 20 \text{ mm}^2$) the visible part of heat-induced delamination was found to be 10,600 Hz and was used for the defect’s resonant excitation. The RACE image (Figure 6b) clearly reproduces the defect size and shape and demonstrates a fairly high ($\approx 20 \text{ dB}$) signal-to-noise ratio (SNR).

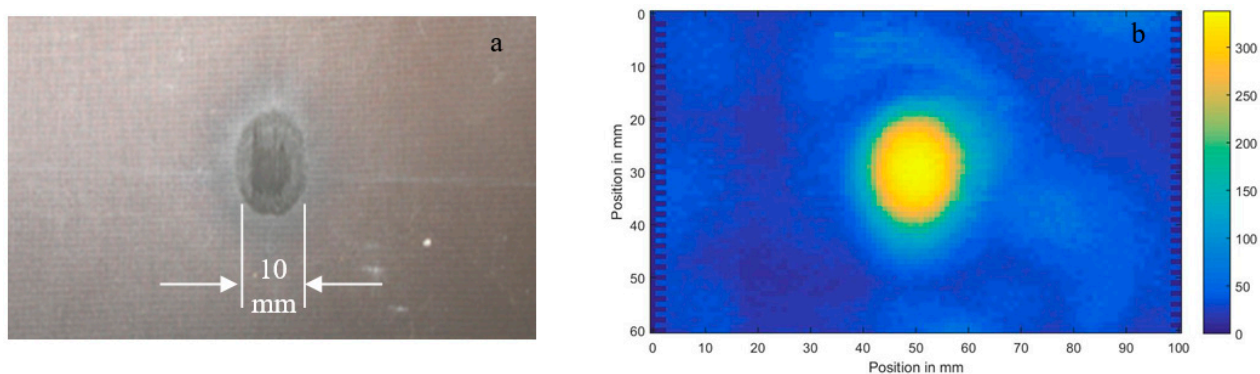


Figure 6. Heat-induced damage in CFRP (a) and its RACE image at LDR frequency 10600 Hz (b).

Figure 7 demonstrates the application of RACE to imaging of hidden defects (20 Joule impact in the non-crimp CFRP plate ($150 \times 100 \times 4.5 \text{ mm}^3$)). The impact produces mainly internal damage that is barely visible (BVID) on the reverse side of the specimen (Figure 7a). The interior damage induced by the impact has a complex structure of multiple delaminations of different sizes and values of LDR frequency [20]. The RACE image obtained at one of the fractional LDR frequencies (18 kHz) is shown in Figure 7b, and evidently depicts complicated defects such as BVID.

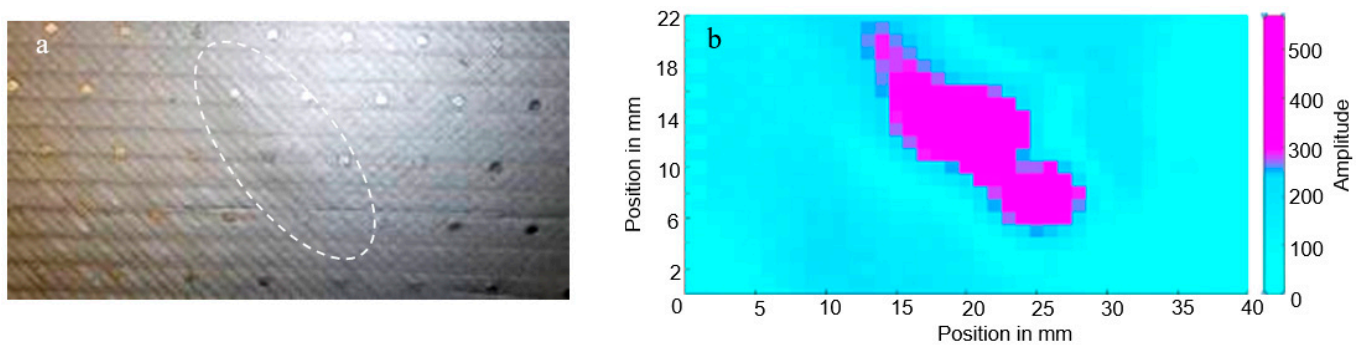


Figure 7. RACE imaging of BVID defect in CFRP plate: (a) photo of the defect; (b) AE scanning image.

The case studies presented above are based on preliminary measurements of LDR frequency, which are then used for a monochromatic, resonant activation of defects. To avoid additional vibrometry measurements of LDR frequency, a wideband (1–100 kHz, noisy signal) excitation can be combined with C-scanning. In this noisy mode, all fundamental and fractional LDR (if they are inside this frequency range) are excited. Since the phases of the excited resonant vibrations are different, the image has a noisy structure.

Two examples illustrating multiple-defect imaging via noisy RACE mode are shown in Figure 8. The white noise input voltage for a vacuum-attached piezo-transducer is produced by an arbitrary signal generator (Stanford research systems Model DS 345) and covers the range 0–20 MHz. Overall acoustic bandwidth generated by the transducer is, however, limited by its frequency response and demonstrates quite an inhomogeneous spectral distribution, mainly within the 100 kHz bandwidth. This bandwidth, nevertheless, covers the fundamental and majority of the higher-order LDR for the specimens studied: a set of four circular FBH (2 cm diameter) and different depths in PMMA (Figure 8a), and four artificial square delaminations ($\sim 27 \times 27 \text{ mm}^2$) at different depths in CFRP plate (Figure 8b). As a result, resonant AE enables us to visualize the defects in a single, noisy-mode experiment without preliminary knowledge of LDR frequencies.

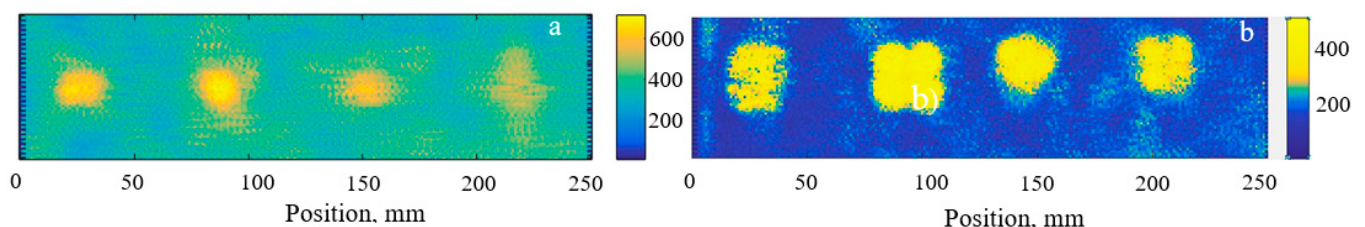


Figure 8. Multiple-defect imaging in noisy mode of RACE: 4 circular FBH of different depths (a) and 4 square inserts at various depths (b) in CFRP plate.

5. Nonlinear AE-Mode

It is well known that planar defects in composites are accompanied by the damage that results from a combination of matrix-fibre debonding, cracking and delaminations. Such a mixture of the fractured constituents makes the defect area highly nonlinear due to contact acoustic nonlinearity (CAN) [21]. Due to CAN, local, nonlinear vibration spectra

acquire a number of new frequency components which are used as sensitive signatures of emerging damage in the nonlinear approach to NDT.

The highly nonlinear vibrations of the defects apparently contribute to the RACE spectrum and bring about the nonlinear AE [22,23]. The experimental setup capable of detecting nonlinear AE and applying it to the imaging of defects (Figure 9) uses a high-frequency (~ 450 kHz (3 dB-bandwidth of ~ 20 kHz)) focused, air-coupled transducer as a receiver. A strong rejection of low-frequency signals used for the defect piezo-excitation is provided by its band-pass frequency response and high-pass filtering circuit. The nonlinear frequency components (higher harmonics (HH)) are then filtered through and used as an input to air-coupled scanning equipment (AirTech 4000) for mapping of the nonlinear components' distributions (C-scan).

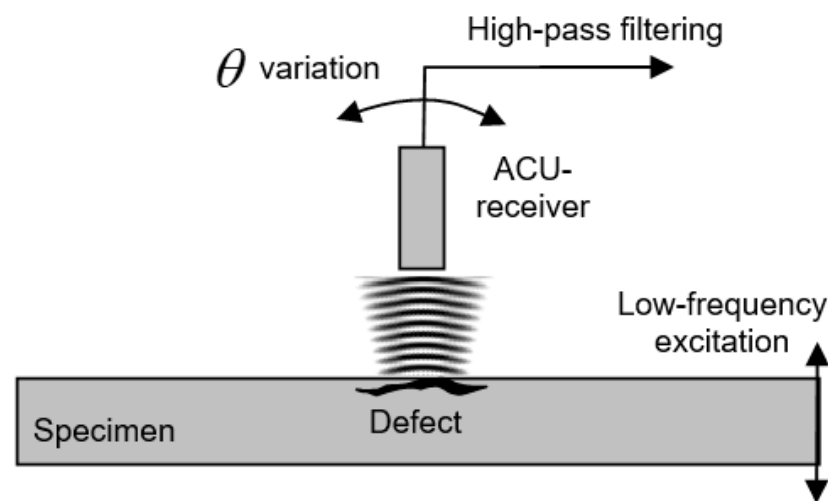


Figure 9. Setup for detecting nonlinear AE and applying it to imaging of defects.

The feasibility of the nonlinear AE is illustrated in Figure 10 for a damaged, glass fibre-reinforced polymer (GFRP) specimen ($2 \times 30 \times 200$ mm³) with an embedded ceramic actuator (“smart structure”). Repetitive voltage application caused an oval delamination between the actuator and the substrate. The nonlinear bandpass spectra of the receiver that contain (2–4) higher-order harmonics were used for nonlinear AE imaging of the delamination and are compared with nonlinear laser vibrometry in Figure 10. Both techniques reliably visualize the delaminated part of the defect with virtually comparable sensitivity and resolution. A certain difference in images is apparently concerned with the different nonlinear outputs used, namely the third harmonic image (~ 58 kHz) in the optical case Figure 10c and (23 + 24) HH (around 450 kHz) AE image Figure 10b.

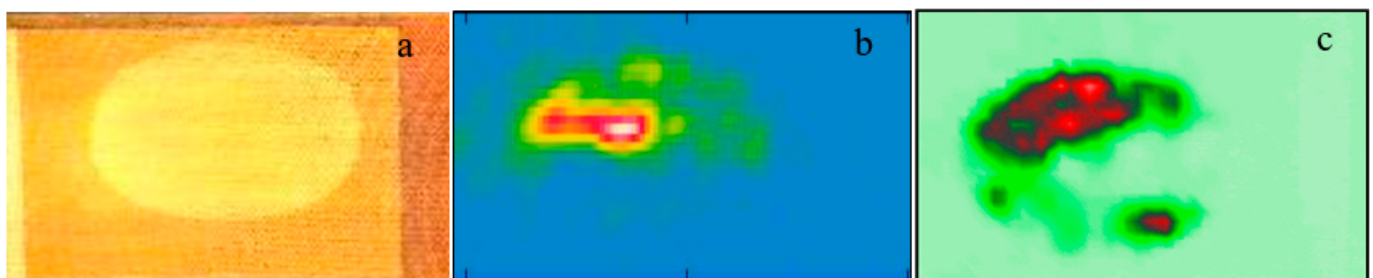


Figure 10. Imaging of the oval delamination (a) in smart structure: nonlinear AE (b) and laser vibrometry image (c).

A high spatial resolution of the nonlinear AE imaging is also demonstrated in Figure 11. The mm-size contour details of the complex shape delamination (5×10 mm², Figure 11a) in the multiplied GFRP are traced closely in the airborne HH image (Figure 11b).

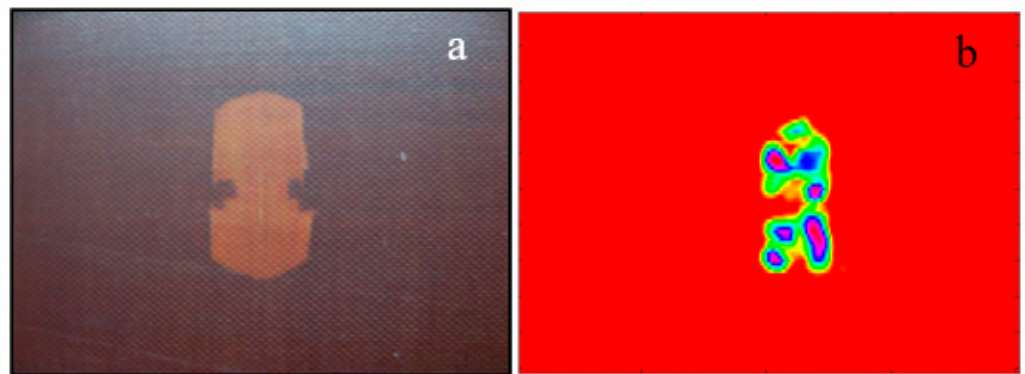


Figure 11. (23 + 24 HH) AE image (b) of the delamination in composite plate (a).

The result in Figure 11 is obtained in nonresonant mode, i.e., the excitation frequency (20 kHz) was quite distant from the defects' LDR frequencies. For this reason, piezo-stack transducers and a high-power supply (Branson, USA) have been applied to generate the nonlinear AE. By combining the resonance conditions provided by LDR with highly efficient CAN, a substantial improvement in the efficiency of nonlinear AE as a signature of cracked defects can be expected.

The LDR-induced increase in local vibration amplitude enables lowering of the excitation level and observation of a highly efficient HH AE at lower acoustic inputs, using conventional ultrasonic equipment. The two examples of resonant HH AE (Figure 12) images are obtained with excitation by low-cost piezo-elements of 2–5 kHz fundamental frequencies, distributed by Conrad Elektronik GmbH. The image of a circular FBH (8 mm diameter, 50 kHz LDR frequency, Figure 12b) is observed at the 9th HH (450 kHz), while for the point impact in CFRP ($\sim 5 \times 5 \text{ mm}^2$, Figure 12c), the output frequency of 440 kHz corresponds to the 4th HH of its LDR frequency, 110 kHz. The high-contrast and signal-to-noise ratio (SNR) HH AE images are comparable with those obtained with laser vibrometry (Figure 12a) and require a few volts of input at most.

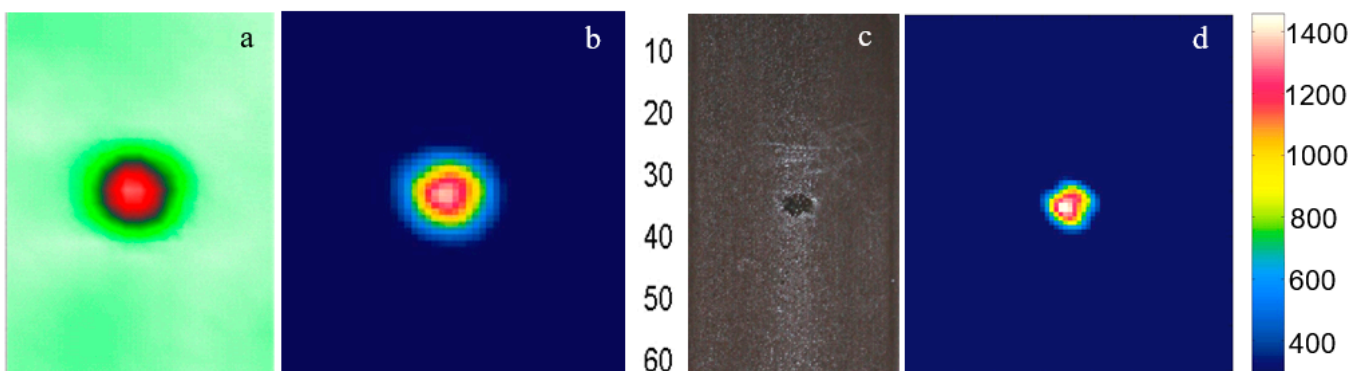


Figure 12. Resonant HH AE images: obtained with laser vibrometry (a); circular FBH in PMMA (b); point impact in CFRP ($\sim 5 \times 5 \text{ mm}^2$) (c); point impact in CFRP (d).

The LDR-induced increase in the nonlinear vibration response can also be applied to observation of the AE-version of another “classical” nonlinear effect of frequency mixing. The method is based on the nonlinear interaction between ultrasonic waves of different frequencies (f_1, f_2) that results in a mixed frequency output: $f_{\pm} = f_1 \pm f_2$.

In the “interacting wave AE amplifier” experiment [24], the LDR-induced “amplification” of the mixed frequency AE was studied for the delamination in the smart structure GFRP (Figure 10a), with LDR frequency $\sim 19 \text{ kHz}$. The two interacting flexural waves were excited in CW-mode by the piezo-transducers attached to the opposite edges of the plate. The frequency-mixed AE signal is received by a microphone positioned at a certain distance

above the delamination. The spectrum of the AE output obtained after FFT for the nonlinear interaction between 19 kHz and 20 kHz primary waves is shown in Figure 13. A highly efficient generation of multiple higher-order mixed frequency components in AE is clearly seen and is due to the combined effect of LDR and CAN. Any of the mixed frequencies are applicable for multiple AE imaging of defects in a single scanning mode [24].

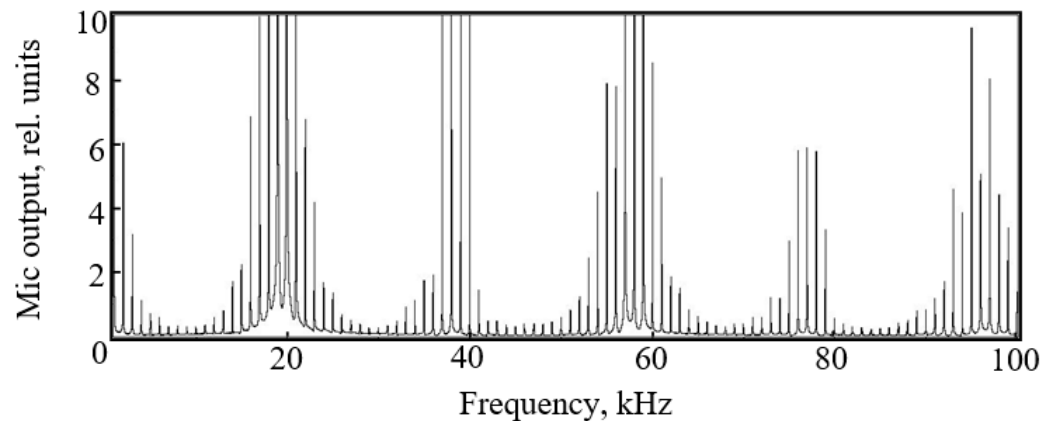


Figure 13. Mixed-frequency resonant AE spectrum for 19 kHz and 20 kHz primary wave interactions.

6. Robotic AE Scanning Mode

Unlike the above-studied RACE scanning of flat specimens, the use of robots combined with optical measurements of the surface profile brings forth imaging of the defects in complicated shape objects. In our experiments, the viability of robotic AE scanning is tested based on the six-axis robot, IRB 120 (ABB, Zürich, Switzerland). To employ the same ultrasound recorder, the robot control unit, IRC 5, was instructed to emulate the encoder signals over IO-card for virtual the y- and z-axes. To detect the AE signal, the microphone, in a special holder, is fastened to the robot flange (Figure 14).

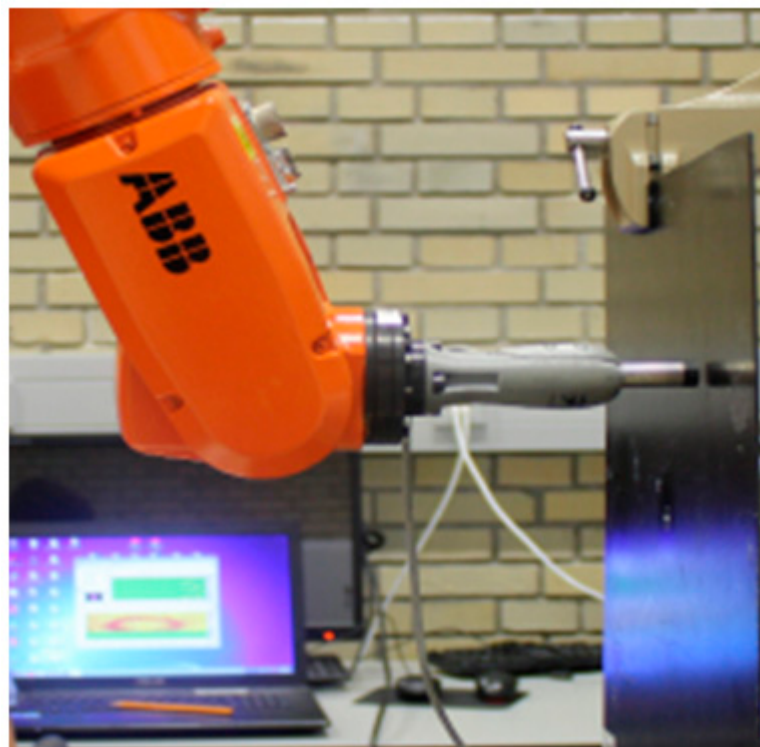


Figure 14. Experimental setup for robotic scanning.

To evade initial seeking for LDR frequency, the wideband, noisy excitation was used in the AE robotic mode. Figure 15b demonstrates the potential of robotic AE imaging for circular FBH in PMMA of equal radii $R = 10$ mm but of different back-wall thicknesses. Therefore, their LDR frequencies are significantly different (from 13,950 Hz to 21,300 Hz). However, the wideband mode enables activation of all of them and contributes to the image obtained by a single C-scan. As seen in Figure 15, similar vibrometry images are of superior quality, nonetheless, the AE images clearly identify the defects.

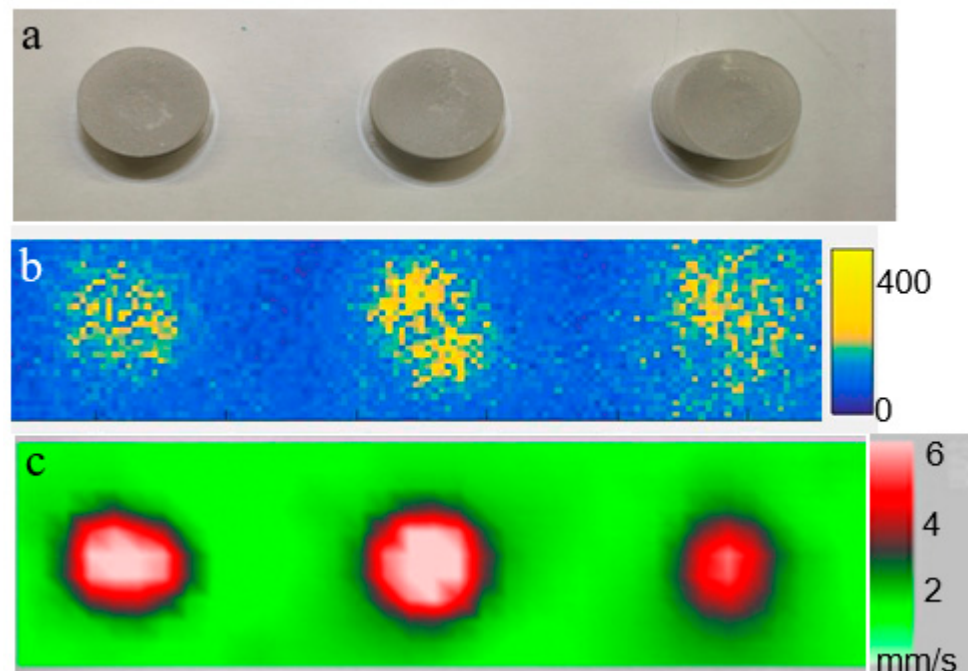


Figure 15. (a) 3 FBH in PMMA; (b) multiple AE images in a single robotic scan in noisy mode; (c) vibrometer image of FBH activated at their LDR frequencies.

As mentioned above, for cm-size defects the fundamental LDR frequencies are in the range of tens of kHz. In the excitation bandwidth employed (~ 100 kHz), multiple higher-order resonances are also activated in addition to the fundamental LDR. They cover the total defect area, and the superimposed multiple-order LDR readily reproduce the shape of the defects [11]. The effect is shown in Figure 16 for a set of four square (20×20 mm²) subsurface inserts in a CFRP plate ($5 \times 290 \times 330$ mm³). The AE robotic mode validates a fair quality of imaging, clearly identifying the shapes, positions and the sizes of the defects.

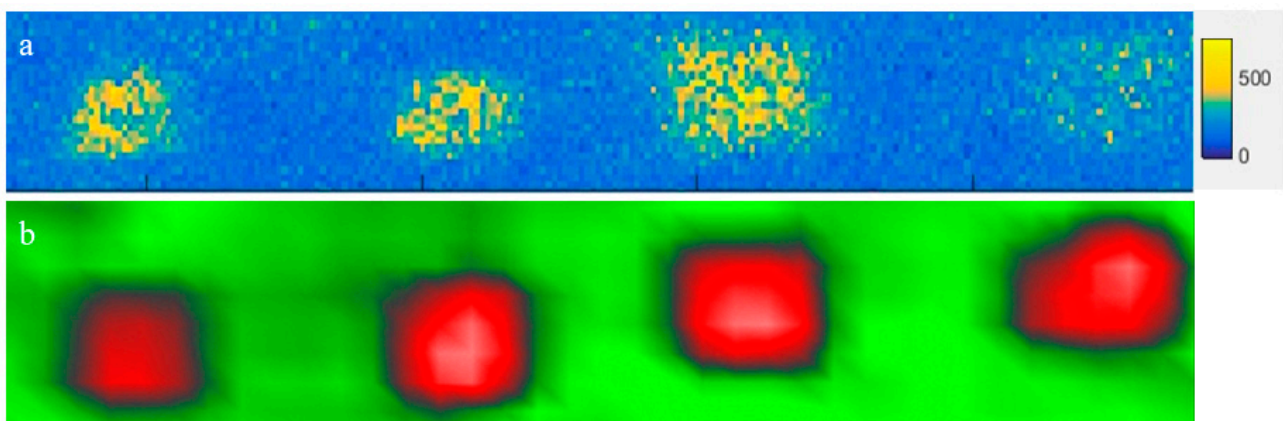


Figure 16. Noisy mode of robotic imaging of 4 square inserts in CFRP plate: AE imaging (a), wideband laser vibrometry (b).

The noisy robotic scanning also works well to visualize the defects of appreciably more complex shapes. This is demonstrated in Figure 17a, where the noisy-mode AE image of the Teflon ring delamination (outer diameter 55 mm) in the CFRP plate ($400 \times 400 \times 2 \text{ mm}^3$) is compared with the laser vibrometry image obtained for (1–100 kHz) excitation Figure 17b. In the ring, the laser vibrometry unfolds a number of fractional LDR in the 10 kHz to 50 kHz range that visualize a particular part of the defect. Their superposition in the wideband AE mode reconstructs the whole picture of the ring delamination.

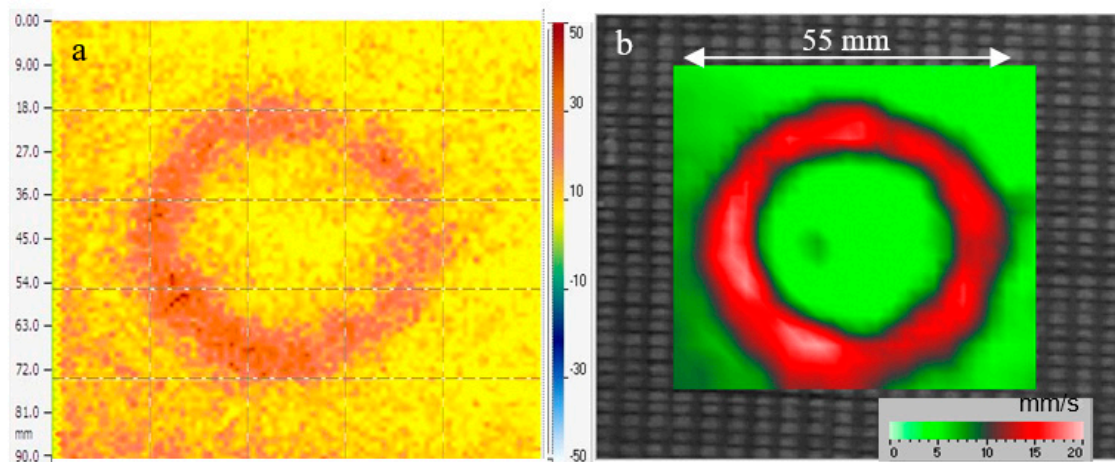


Figure 17. (a) robotic AE image of a ring delamination in CFRP; (b) wideband laser vibrometry image.

7. Full-Field AE Mode Imaging

Despite a reasonable image quality obtained by AE scanning, as displayed above, the technique is relatively time consuming. For instance, for the scanning speed of 10 mm/s, it took from 10 to 20 min to scan the area of the defects in the above experiments. To avoid this drawback, a new full-field AE imaging method is developed that applies acoustic cameras for instant detection and imaging of the defects.

The viability of the method is elucidated below by experimenting with an acoustic camera SoundCam by CAE systems, Gütersloh, Germany. It includes 64 MEMS-microphones, the 24-bit acquisition system of sampling rate 48 kHz, and an operating frequency range 10 Hz–24 kHz. The experimental setup for full-field AE imaging with this camera is shown in Figure 18. The operation parameters include adjustment of the distance, dynamic range and the frequency of the receiver.

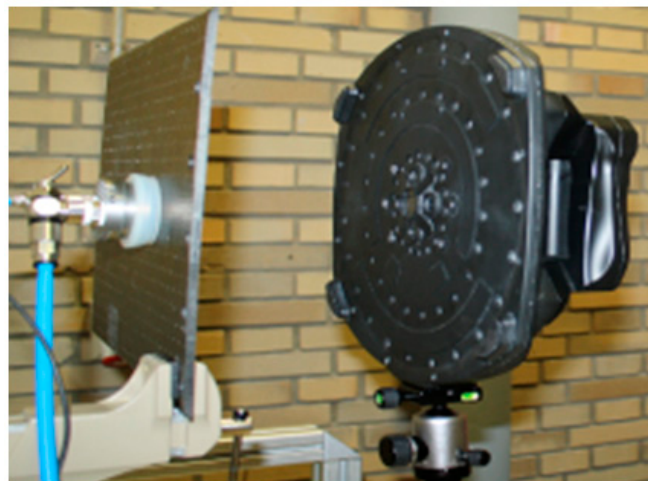


Figure 18. SoundCam setup for full field AE imaging.

To test its performance, the airborne acoustic radiation of the piezo-actuator was imaged first (Figure 19). As seen, the radiation circular part of the transducer (diameter ~ 5 mm) is clearly spotlighted in the image. The SoundCam interface in Figure 19 also indicates a fairly high (>10 dB) dynamic range of the image and displays the frequency radiated ($\approx 13,100$ Hz).

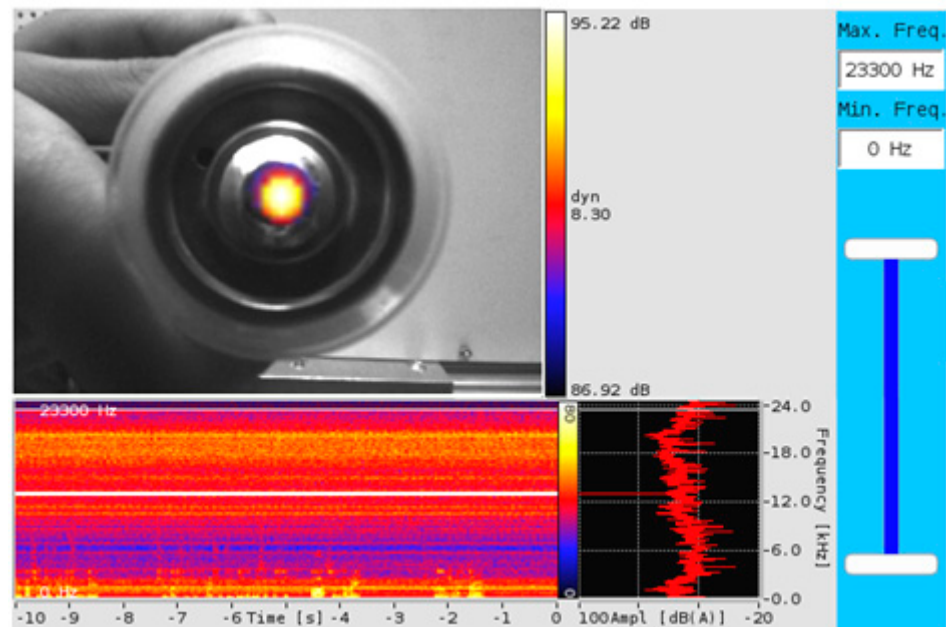


Figure 19. The SoundCam interface and full-field image of airborne radiation from piezo-actuator (frequency 13,100 Hz).

The noisy mode of the transducer was then used for imaging of AE excitation from a pair of FBH of slightly different LDR frequencies (12,200 Hz and 13,300 Hz), (Figure 20). To distinguish between these frequencies of the radiation, the bandwidth of the SoundCam was packed closely to the values of the LDR frequencies (12,200 and 13,300 Hz, Figure 20d) to demonstrate successive frequency-selective AE imaging of the defects.

The full-field mode operates well for the imaging of real defects in composites, as demonstrated in Figure 21a,b, for the delamination in the actuator imbedded in the GFRP plate. The defect is easily seen in the laser vibrometry image at LDR frequency 18,900 Hz (Figure 21b). The full-field AE image obtained at this frequency (Figure 21a) indicates the resonance part of the delamination, but provides essentially instant testing.

Figure 22 shows a few other examples of acoustic camera imaging for impact-induced damage in CFRP. The damage in the stringer-reinforced CFRP specimen results in a visible crack on the reverse side (Figure 22a) that is evident in the laser vibrometry image at LDR frequency 17,940 Hz (Figure 22c). Instead, the AE image detected by the acoustic camera reveals the sound radiation from the vibrating edges of the defect only (Figure 22b). The AE image of the crack is thus similar to the full field ultrasonic thermography image [25], where the vibration of the crack tips results in a strong energy dissipation and maximal temperature rise.

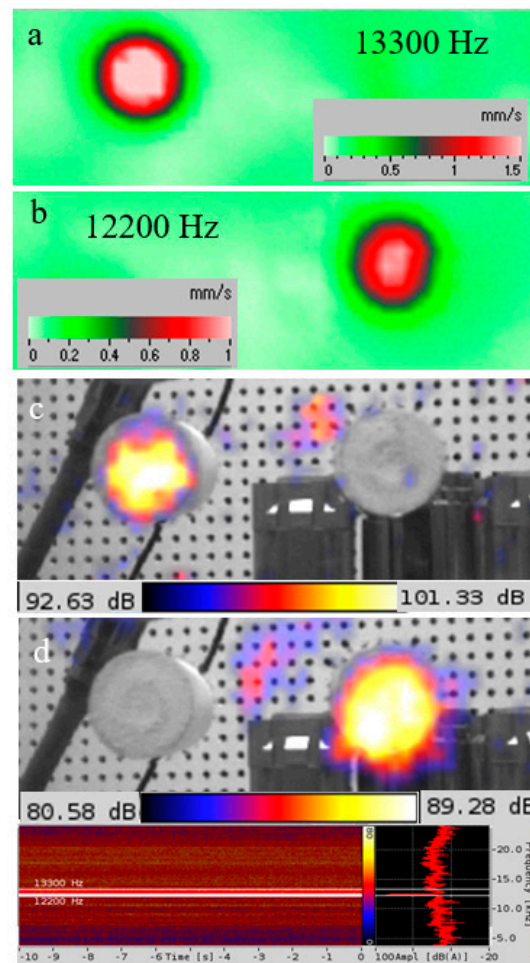


Figure 20. Laser vibrometry (a,b) and frequency-selective full-field AE imaging (c,d) of a pair of circular FBH of close LDR frequencies.

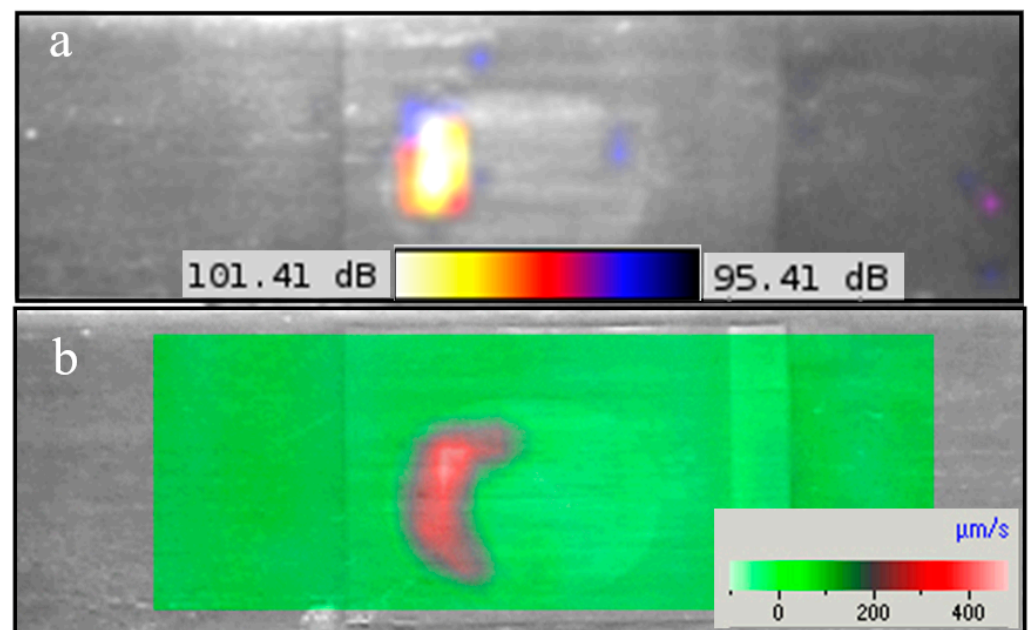


Figure 21. Soundcam imaging of a delamination in piezo-actuator imbedded in GFRP plate (a), 18,900 Hz LDR laser vibrometry image of the delamination (b).

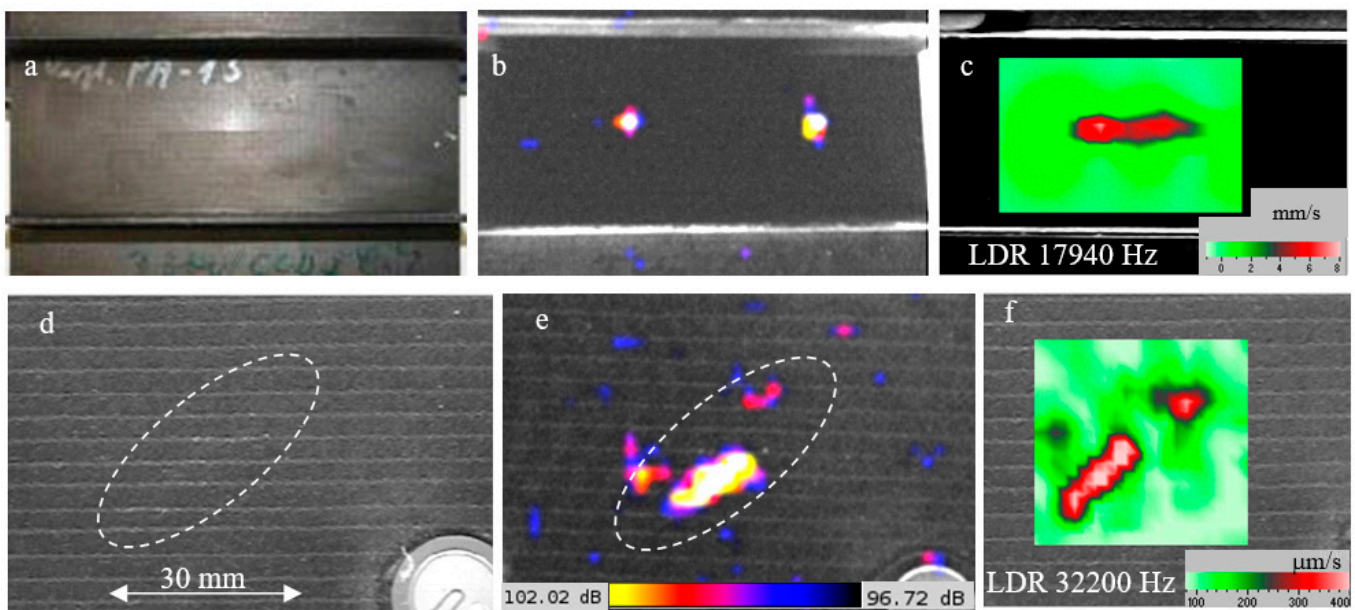


Figure 22. (a) crack in CFRP stringer-reinforced sample, SoundCam image (b), laser vibrometer LDR image (c); (d) BVID in non-crimp fabric CFRP; fractional LDR 32,200 Hz vibrometry image (f) and full-field AE image using acoustic camera (e).

The AE imaging of a hard-to-detect BVID (Figure 22d) induced by a 20 Joule-impact in non-crimp fabric CFRP sample ($150 \times 100 \times 3 \text{ mm}^3$) is illustrated Figure 22. The laser vibrometry proves multiple fractional LDR of the damage that lie in a reasonably high frequency range (above the frequency range of the acoustic camera), e.g., at LDR frequency 32,200 Hz (Figure 22f). Despite this value being above the maximal frequency of the SoundCam, the camera still provides a fair AE image of the hidden defect, and evidently relays the presence and the position of the damage in the noisy mode (Figure 22e).

8. Conclusions

Resonant airborne emission is the effect of acoustic waves generated from the defect area in ambient air by local standing wave vibrations developed in this area at LDR frequency. A monochromatic, resonant activation of defects substantially enhances the efficiency of AE, which is readily detected by a commercial microphone or an air-coupled transducer. An approach which does not require preliminary knowledge of LDR frequency is one based on wideband acoustic activation by using a noise-like input signal. The FFT of the signal obtained in the noisy activation mode resolves the inverse problem of finding LDR frequencies.

The AE field from the defect area is a footprint of the radiation source, and thus is applicable to AE detection and imaging of defects in composites via microphone C-scanning of the specimens. The quality of the resonant AE images is comparable with the images obtained via scanning laser vibrometry. Activation of LDR in combination with high nonlinearity of cracked defects in composites greatly increases the nonlinear AE of defects in the form of the higher harmonics and mixed frequencies. The noisy mode provides full-scale imaging of the shape of the defect due to excitation of the higher-order LDR.

Unlike conventional AE scanning of flat composite plates, the use of robots brings forth an opportunity for detecting and imaging of the defects in complicated-shape objects. The robotic AE scanning mode supplemented with noisy excitation enables imaging of multiple defects without a prior search for LDR frequencies. A newly developed full-field AE imaging method based on commercial acoustic cameras changes a slow and tedious scanning operation into a rapid visualization of defects. Multiple case studies of the full-field AE approach validate the reliable imaging of various risk defects in composites. The

resonant AE approach simplifies integration of the proposed NDT imaging system, which includes inexpensive, fully acoustic, instrumental components.

Author Contributions: I.S. implemented the major bulk of the RACE analysis and measurements in the scanning mode. Y.B. was responsible for the robotic and the full-field modes. M.K. initiated and coordinated experimental work and perception of the results. All authors have read and agreed to the published version of the manuscript.

Funding: This research was funded by DFG, grant number KR 31 2131/12-1.

Institutional Review Board Statement: Not applicable.

Informed Consent Statement: Not applicable.

Data Availability Statement: The data presented in this study are available in references [8,9,16,18–24].

Acknowledgments: The authors acknowledge funding of this study in the framework of DFG project KR 31 2131/12-1.

Conflicts of Interest: The authors hereby declare that the submitted work was carried out in the lack of any personal, professional or financial relationships that could potentially be considered as a conflict of interests.

Abbreviations

LDR	Local Defect Resonance
RACE	Resonant Air-Coupled Emission
AE	Acoustic Emission
NDT	Nondestructive Testing
FBH	Flat Bottom Hole
FEM	Finite Element Method
PMMA	Polymethyl Methacrylate
CFRP	Carbon Fibre-Reinforced Polymer
RMS	Root Mean Square
SNR	Signal-To-Noise Ratio
BVID	Barely Visible Damage
CAN	Contact Acoustic Nonlinearity
HH	Higher Harmonics
GFRP	Glass Fibre-Reinforced Polymer
FFT	Fast Fourier Transform

References

- Witten, E.; Mathes, V.; Sauer, M.; Kühnel, M. *Composites-Marktbericht*; Federation of Reinforced Plastics: Frankfurt am Main, Germany, 2018.
- Wevers, M.; Surgeon, M. Acoustic Emission and Composites. *Compr. Compos. Mater.* **2000**, *5*, 345–357. [[CrossRef](#)]
- McLaskey, G.C.; Glaser, S.D.; Grosse, C.U. Beamforming array techniques for acoustic emission monitoring of large concrete structures. *J. Sound Vib.* **2010**, *329*, 2384–2394. [[CrossRef](#)]
- Matsuo, T.; Hatanaka, D. Development of non-contact fatigue crack propagation monitoring method using air-coupled acoustic emission system. *Eng. Trans.* **2019**, *67*, 185–198. [[CrossRef](#)]
- Acoustic Camera/Sound Source Localization-Noise Inspector. Available online: <https://www.cae-systems.de> (accessed on 10 October 2021).
- Movahed, A.; Waschkies, T.; Rabe, U. Air Ultrasonic Signal Localization with a Beamforming Microphone Array. *Adv. Acoust. Vib.* **2019**, *2019*, 1–12. [[CrossRef](#)]
- Pfeiffer, H.; Böck, M.; Pitropakis, I.; Szewieczek, A.; Hillger, W.; Glorieux, C. Identification of impact damage in sandwich composites by acoustic camera detection of leaky Lamb wave mode conversions. *e-J. Nondestruct. Test.* **2013**, 1435–4934.
- Solodov, I.; Bai, J.; Bekgulyan, S.; Busse, G. A local defect resonance to enhance acoustic wave-defect interaction in ultrasonic nondestructive evaluation. *Appl. Phys. Lett.* **2011**, *99*, 211911. [[CrossRef](#)]
- Solodov, I.; Dillenz, A.; Kreutzbruck, M. A new mode of acoustic NDT via resonant air-coupled emission. *J. Appl. Phys.* **2017**, *121*, 245101. [[CrossRef](#)]
- Hettler, J.; Tabatabaeipour, M.; Delrue, S.; Abeele, K.V.D. Detection and Characterization of Local Defect Resonances Arising from Delaminations and Flat Bottom Holes. *J. Nondestruct. Eval.* **2017**, *36*, 2. [[CrossRef](#)]

11. Rahammer, M.; Kreutzbruck, M. Fourier-transform vibrothermography with frequency sweep excitation utilizing local defect resonances. *NDT E Int.* **2017**, *86*, 83–88. [[CrossRef](#)]
12. Fierro, G.P.M.; Ginzburg, D.; Ciampa, F.; Meo, M. Imaging of Barely Visible Impact Damage on a Complex Composite Stiffened Panel Using a Nonlinear Ultrasound Stimulated Thermography Approach. *J. Nondestruct. Eval.* **2017**, *36*, 69. [[CrossRef](#)]
13. Pieczonka, L.; Zietek, L.; Klepka, A.; Staszewski, W.; Aymerich, F.; Uhl, T. Damage imaging in composites using nonlinear vibro-acoustic wave modulations. *Struct. Control. Health Monit.* **2017**, *25*, e2063. [[CrossRef](#)]
14. Segers, J.; Kersemans, M.; Hedayatrasa, S.; Calderon, J.; Van Paepegem, W. Towards in-plane local defect resonance for non-destructive testing of polymers and composites. *NDT E Int.* **2018**, *98*, 130–133. [[CrossRef](#)]
15. Roy, S.; Bose, T.; Debnath, K. Detection of local defect resonance frequencies using bicoherence analysis. *J. Sound Vib.* **2019**, *443*, 703–716. [[CrossRef](#)]
16. Solodov, I.; Rahammer, M.; Kreutzbruck, M. Analytical evaluation of resonance frequencies for planar defects: Effect of a defect shape. *NDT E Int.* **2019**, *102*, 274–280. [[CrossRef](#)]
17. Viktorov, I.A. *Rayleigh and Lamb Waves: Physical Theory and Applications*; Springer: New York, NY, USA, 1967.
18. Solodov, I.; Döring, D.; Busse, G. Air-coupled laser vibrometry: Analysis and applications. *Appl. Opt.* **2008**, *48*, C33–C37. [[CrossRef](#)] [[PubMed](#)]
19. Bernhardt, Y.; Solodov, D.; Müller, D.; Kreutzbruck, M. Listening for Airborne Sound of Damage: A New Mode of Diagnostic Imaging. *Front. Built Environ.* **2020**, *6*, 66. [[CrossRef](#)]
20. Solodov, I. Nonlinear Acoustic Measurements for NDE Applications: Waves versus Vibrations. In *Measurement of Nonlinear Ultrasonic Characteristics*; Jhang, K.Y., Lissenden, C., Solodov, I., Ohara, Y., Gusev, V., Eds.; Springer: Singapore, 2020; pp. 111–164.
21. Solodov, I.; Krohn, N.; Busse, G. CAN: An example of nonclassical acoustic nonlinearity in solids. *Ultrasonics* **2002**, *40*, 621–625. [[CrossRef](#)]
22. Solodov, I.; Busse, G. Nonlinear air-coupled emission: The signature to reveal and image microdamage in solid materials. *Appl. Phys. Lett.* **2007**, *91*, 251910. [[CrossRef](#)]
23. Solodov, I. Nonlinear Acoustic Response of Damage Applied for Diagnostic Imaging. In *Nonlinear Ultrasonic and Vibro-Acoustical Techniques for Nondestructive Testing*; Kundu, T., Ed.; Springer: Cham, Switzerland, 2019; pp. 301–343.
24. Solodov, I.; Kreutzbruck, M. Ultrasonic frequency mixing via local defect resonance for defect imaging in composites. *Ultrasonics* **2020**, *108*, 106221. [[CrossRef](#)] [[PubMed](#)]
25. Stoessel, R.; Dillenz, A.; Krohn, N.; Busse, G. Zerstörungsfreie Prüfung mit defekt-selektiven Abbildungsverfahren. *Materialprüfung* **2000**, *42*, 38–44.